Modelling diamond-like carbon with the environment-dependent interaction potential

2002 J. Phys.: Condens. Matter 14 2901

(http://iopscience.iop.org/0953-8984/14/11/308)

INSTITUTE OF PHYSICS PUBLISHING JOURNAL OF PHYSICS: CONDENSED MATTER

J. Phys.: Condens. Matter **14** (2002) 2901–2927 PII: S0953-8984(02)28377-0

Modelling diamond-like carbon with the environment-dependent interaction potential

Nigel Marks

School of Physics, The University of Sydney, NSW 2006, Australia

E-mail: nigel@physics.usyd.edu.au

Received 6 August 2001, in final form 13 November 2001
Published 8 March 2002
Online at stacks.iop.org/JPhysCM/14/2901

Abstract

The environment-dependent interaction potential is a transferable empirical potential for carbon which is well suited for studying disordered systems. *Ab initio* data are used to motivate and parametrize the functional form, which includes environment-dependence in the pair and triple terms, and a generalized aspherical coordination describing dihedral rotation and non-bonded π-repulsion. Simulations of liquid carbon compare very favourably with Car–Parrinello calculations, while amorphous networks generated by liquid quench have properties superior to Tersoff, Brenner and orthogonal tight-binding calculations. The efficiency of the method enables the first simulations of tetrahedral amorphous carbon by deposition, and a new model for the formation of diamond-like bonding is presented.

1. Introduction

First reported in 1991 [1], tetrahedral amorphous carbon (ta-C) is an amorphous diamond-like material prepared by various apparatus such as filtered cathodic arc [2], mass-selected ion beam [3], ion-assisted deposition [4] and magnetron sputtering [5]. The diamond-like properties of ta-C arise from the tetrahedral (sp^3) bonding which in crystalline form gives diamond the highest hardness and thermal conductivity of any material and a bandgap of 5.1 eV. In the case of ta-C the sp^3 fraction can be as high as 80–85%, leading to a structure which is also extremely hard, is a weak p-type semiconductor with an optical gap of 2 eV and has excellent wear-resistance. These properties have led to numerous applications in coating technology, the most visible of which is the new generation of diamond-like blades.

The absence of crystalline order in ta-C leads to ambiguity in experimental characterization, and thus atomistic simulation has an important role to play in the determination of physical and electronic microstructure. Simulation studies are also crucial to address questions of dynamics. The most significant mechanism to identify is the deposition process responsible for the tetrahedral bonding, with a variety of theories proposed

including subplantation (the dominant view) [6–8], the cylindrical thermal spike [9], atomic peening [10] and compressive stress promotion [11]. Another important experimental result not yet understood is how intrinsic compressive stress is annealed without reducing the sp^3 fraction [12, 13].

The principal challenge in the simulation of ta-C is transferability, since the amorphous network contains multiple hybridizations in highly strained environments which lie far from the idealized arrangements of a molecule or crystal. The ta-C system thus provides a stringent test of the quality of the interaction potential, and in many ways the study of ta-C by simulation is a mutually beneficial exercise. In terms of transferability the preferred techniques are those based upon density-functional theory (DFT), but accuracy is not the only requirement, as the experimental process which forms ta-C is one of ion beam deposition, whereby individual energetic ions arrive at a surface to build up a thin film in an atom-by-atom manner. Simulations of this type require considerable numbers of atoms ($\sim 10^3$) and long simulation times ($\sim 10^6$ steps), and thus are only feasible with less expensive techniques. The challenge in modelling ta-C therefore is to find an interatomic potential capable of describing highly strained interactions, while remaining sufficiently efficient to allow the study of large systems and long times.

While many different levels of theory have been applied to ta-C, almost all fail to satisfy the dual requirements of transferability and efficiency required to model the deposition process. Instead, the most transferable methods have been applied in liquid-quench simulations which neglect surface properties and formation mechanisms. Liquid-quench studies using DFT [14], local basis density functional (LBDF) [15] and non-orthogonal tight-binding (NOTB) [16] have all had considerable success in describing the nature of ta-C, and some of the key results from these simulations are summarized in section 2. Less accurate methods such as orthogonal tight-binding (OTB) [17, 18], and the empirical potentials of Tersoff [19], Brenner [20] and Stillinger–Weber (SW) [21, 22], have provided a poor description of ta-C, but all attempts to model thin-film deposition have used one of these simpler techniques, and these simulations represent an important point of reference which is also reviewed in section 2. Another important carbon simulation method is the environment-dependent OTB approach which introduces coordination-dependent matrix elements [23], while an analytic approximation to the tight-binding bond order potential (BOP) has been developed for hydrocarbons [24]. A further variant of analytic BOP incorporating environment dependence has also been reported [25].

This article reviews and reports on a new carbon empirical potential [26] which for the first time satisfies both the transferability and efficiency criteria. With this potential the first simulations of ta-C thin-film deposition are made possible, providing a range of new insights. Known as the environment-dependent interaction potential (EDIP), this new potential is based upon a related EDIP functional form developed for silicon two years prior [27]. Silicon EDIP was derived by the inversion of *ab initio* cohesive energy curves, providing much improved transferability relative to other empirical potentials, and is the first empirical model to realistically simulate quenching of amorphous silicon from the melt. The carbon form of EDIP is a significant development, overcoming the most significant weakness of silicon EDIP, namely the absence of π-bonding effects. With this improvement important phenomena such as dihedral rotation penalties and π-repulsion are described. In parametrizing the carbon EDIP an emphasis is also placed on transparency, with almost all parameters determined using high-symmetry configurations to isolate functionality.

The functional form of carbon EDIP (subsequently referred to as EDIP) is reviewed in section 3, and includes a particular emphasis on Hartree–Fock (HF) and DFT data used to motivate the functional form and determine its parametrization. In section 4 the predictive power of EDIP is demonstrated in simulations of liquid quenching and thin-film deposition.

A high level of transferability is found in both the liquid and amorphous state, and the deposition simulations reveal that the growth mode for ta-C is not as previously imagined. Section 5 considers future directions.

2. An overview of carbon simulations

The key ingredient in the experimental synthesis of ta-C is the energetic beam, with low- and high-energy beams resulting in low-density amorphous carbon (a-C), but an optimal energy window of 30–200 eV leads to the formation of ta-C with a typical density of 3.0 g cm^{-3}. The impact of each energetic ion generates a molten region (or thermal spike) which cools rapidly due to the high thermal conductivity of dense carbon. Molecular dynamics simulations of ta-C thus divide into two categories, either simulating many hundreds of individual impacts to deposit a film, or considering only the process of melting and rapid cooling. The following discussion presents some of the key results from these deposition and liquid-quench simulations.

2.1. Liquid-quench simulations

Thermal spikes are a key concept in the study of ta-C, providing a *post hoc* justification for the technique of liquid quenching in which a molten sample containing ∼100 atoms is cooled to room temperature in ∼1 ps to form an amorphous solid. Liquid quenching was for some time considered a computational device with little physical relevance, a 1997 analysis [28] demonstrated that the energetic beams used to deposit ta-C generate thermal spikes of sub-picosecond duration and contain 50–100 atoms. Liquid quenching thus provides a computationally expedient and physically reasonable method of simulating the bulk structure of amorphous carbon networks.

The first liquid-quench simulations of ta-C were undertaken in 1993, with three groups applying varying levels of theory. Stephan and Haase [29] applied the simplest approach, using the Tersoff potential in simulations at 2, 2.5 and 3 g cm^{-3}, and found sp^3 fractions of 7, 16 and 34% respectively. Wang and Ho [30] performed OTB simulations, and observed a similar underprediction at 3 g cm^{-3}, finding just 33% sp^3 sites and even a small number (2.3%) of two-coordinate atoms. The first successful description of ta-C arrived with NOTB simulations performed by the group of Frauenheim [31], who observed 53% sp^3 bonding in a 3 g cm^{-3} systems of 64 atoms, and 64% sp^3 bonding in later simulations using 128 atoms. At densities of 3.0 and 3.3 g cm^{-3} they found a π–π^* gap of 3 eV. In 1994 LBDF calculations were performed by Drabold *et al* [32] who simulated a 3 g cm^{-3} structure with an sp^3 fraction of 85%. They also observed that the sp^2 atoms paired up, and found a defect-free gap 2 eV in width.

Car–Parrinello molecular dynamics (CPMD) [33] calculations of ta-C were first presented in 1996 by Marks *et al* [34] who reported a 64-atom 2.9 g cm^{-3} structure containing 65% sp^3 bonding. These simulations observed three- and four-membered rings in the ta-C network, with the former particularly unexpected having not been observed in the tight-binding simulations. Support for the small rings came from several sources including Car–Parrinello (CP) simulations by Crain *et al* [35] and a fingerprint peak for four-membered rings in neutron diffraction data [34]. Annealing of the 3.0 g cm^{-3} LBDF structure using CP simulation saw the appearance of a three-membered ring and a drop in sp^3 fraction to 70% [36], while more recent 125-atom CPMD simulations by McCulloch *et al* [37] found that three- and four-membered rings were present at four different densities between 2.0 and 3.2 g cm^{-3}. Shultz *et al* [38] also considered hypothetical crystal structures in which each atom was situated in a ring of length three or four, and showed that the strain energy was not excessive. The same authors also showed that minimal basis sets and approximate Hamiltonians discriminate

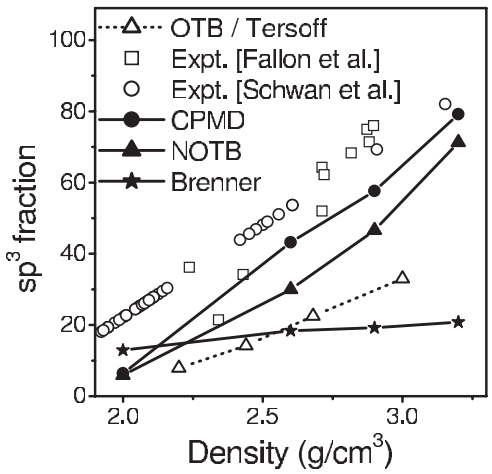

Figure 1. The sp^3 fraction plotted as a function of density. Filled symbols indicate the CPMD, NOTB and Brenner results from [39] calculated using identical preparation conditions. Open circles are experimental results from argon/carbon magnetron-sputtered amorphous carbon [5]. Open squares are experimental values from ion-beam-deposited amorphous carbon [2]. Open triangles indicate the OTB calculations of Wang and Ho [30]. Simulations using the Tersoff potential overlay the OTB data almost exactly [29].

against three-membered rings, thus explaining their observation only in CP simulations with large plane-wave cutoffs.

Direct comparison of the transferability of the various methods applied to ta-C has been clouded by the use of different system sizes, quench rates and definitions of coordination. To resolve this uncertainty a recent comparison of methods was performed [39] in which 125-atom amorphous carbon structures were generated by liquid quench at different densities using preparation conditions as identical as possible. Figure 1 shows the variation in the sp^3 fraction with density, indicating a good correlation between the level of theory and agreement with experiment. In particular, it is apparent that the less computationally expensive methods of OTB and the Tersoff and Brenner potentials are unsuitable for describing the high density of ta-C. However, with regard to the simulation of thin-film deposition, these are the only methods of figure 1 for which the calculations are practical.

2.2. Deposition simulations

The first simulations of carbon deposition used the Tersoff potential and were performed by Kaukonen and Niemenen in 1992 [40]. The calculations followed the full motion of only the ten fastest moving atoms, and in these approximate simulations a maximum sp^3 fraction of 44% was found for films grown with a 40 eV beam. In 1996 Marks *et al* [21] simulated the growth of two-dimensional carbon films using a graphitic SW potential and in agreement with experiment found a maximum in the compressive stress as a function of the incident ion energy. Another approximate study of carbon deposition by Uhlmann *et al* [41] used NOTB to follow the impact of a small number of energetic ions ($\sim$20) onto an amorphous carbon surface generated by liquid quenching. These studies provided the first tight-binding insight into carbon impact process and found that subplantation processes absent in the two-dimensional SW simulations are present in three dimensions.

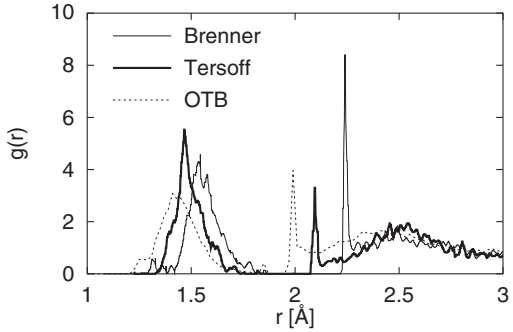

Figure 2. Pair correlation function $g(r)$ from film deposition simulations using the Tersoff [43], modified Brenner [43] and truncated OTB methods [44]. Deposition energies were 40, 40 and 100 eV respectively.

The first true three-dimensional simulations of thin-film carbon deposition did not appear until 2000 when Tersoff, Brenner and OTB simulations were performed. Kaukonen and Niemenen [42] performed new simulations using the Tersoff potential, and found thin-film structures with sp^3 bonding fractions no greater than 29%, in poor agreement with experiment, but consistent with the liquid-quench calculations of Stephan and Haase [29]. The highest density (3.03 g cm^{-3}) was observed for films deposited with 40 and 100 eV atoms, but these structures contained just 26 and 24% sp^3 bonding respectively. Jäger and Albe [43] deposited carbon films using the Tersoff and Brenner potentials and found 3 g cm^{-3} structures with sp^3 fractions of 34 and 3% respectively. Further simulations incorporating *ad hoc* modifications to the cutoff function of the Brenner potential led to structures with 85% sp^3 bonding at the expense of an unphysical spike in the radial distribution function (RDF) as shown in figure 2. The Tersoff simulations of [43] show a similar spike, indicating an significant accumulation of atoms which is unphysical and inconsistent with experiment. Fagan *et al* [44] deposited a film using OTB with an incident ion energy of 100 eV, and for reasons of computational efficiency the interaction was splined to zero at 2.0 Å. As for the modified Brenner potential, a substantial spike in the RDF is observed at the cutoff distance. Furthermore, the sp^3 fraction of the OTB film was just 20%, even though the film density was 3.4 g cm^{-3}. While not a simulation of ta-C, the OTB simulations of low-density carbon by Kohary and Kugler [45] are notable as the first successful tight-binding simulations of carbon thin-film growth.

The inconsistency between density and sp^3 fraction is a characteristic of potentials which do not properly describe non-bonded π-repulsion. This shortcoming is most apparent for graphite, where neglecting the repulsion between non-bonded sp^2 sites leads to a representation of graphite with a density approaching (or even exceeding) the diamond density of 3.5 g cm^{-3}, whereas in fact the true density of graphite is 2.27 g cm^{-3} due to the spacing of 3.35 Å between sheets. The origin of the high-density, low-sp^3 behaviour in these simulations is thus attributable to the short range of the interaction, where the location of cutoff is identified by the sharp leading edge of the spikes in figure 2. This second deficiency reflects the *ad hoc* description of the interaction cutoff itself. Two of the defining characteristics of EDIP are its treatment of non-bonded π-repulsion and the DFT-derived coordination cutoff, and these properties give EDIP excellent transferability as seen in section 4.

3. The environment-dependent interaction potential—EDIP

The functional form of EDIP consists of three components: a two-body pair energy, a three-body angular penalty and a generalized coordination. Within this framework the total energy

is written as a sum of on-site energies U_i given by

$$U_i = \sum_j U_2(r_{ij}, Z_i) + \sum_{j<k} U_3(r_{ij}, r_{ik}, \theta_{jik}, Z_i) \tag{1}$$

where i is the on-site species, and j and k are neighbours. The coordination Z_i has in general a fractional value and consists of two components, a spherical contribution z_i as found in silicon EDIP, and an aspherical term unique to the carbon potential which is vital for describing distorted configurations involving π-electrons. In highly symmetric configurations as found in graphite, diamond and linear chains the aspherical term vanishes, the spherical term counts precisely the number of nearest neighbours and the coordination then assumes its intuitive integer value.

3.1. Pair interaction

The pair potential U_2 resembles the SW potential [46] in being short ranged, decaying to zero at a distance set by the denominator in the exponential term. For distances smaller than this cutoff the functional form is

$$U_2(r, Z) = \varepsilon\left[\left(\frac{B}{r}\right)^4 - \mathrm{e}^{-\beta Z^2}\right]\exp\left(\frac{\sigma}{r - a - a'Z}\right). \tag{2}$$

The exponential term in $-\beta Z^2$ describes the bond-order and is one of the key innovations in the silicon EDIP functional form. This term moderates the balance between attraction and repulsion as originally proposed by Abell [47], and as implemented in the Tersoff and Brenner potentials. The difference in the case of EDIP is that the form of the bond-order term is derived using the method of inverting *ab initio* cohesive energy curves, and this theoretical grounding is one of the principal sources of transferability in the EDIP pair potential.

The variable cutoff controlled by the parameter a' is absent in silicon EDIP, and plays an important role in the description of carbon. The requirement for a variable cutoff was deduced from HF cluster data used for the parametrization of the pair potential. The HF calculations for sp^2- and sp^3-bonded carbon were performed separately by Bensan [21] and Mahon [22] in order to parametrize SW potentials for graphite (SW3) and diamond (SW4) respectively. It was noted by Bensan that the two pair potentials reduce to a common form when rescaled by the bond-strength and bond-length, and thus it follows a' should be non-zero and positive, indicating an interaction cutoff increasing with coordination according to the fractional difference between the nearest neighbours in diamond and graphite.

The generality suggested by the common reduced SW form was exploited in a rescaling of the HF data using experimental cohesive energies and bond-lengths (graphite, $U_0 = 7.37$ eV and $R_0 = 1.421$ Å; diamond, $U_0 = 7.35$ eV and $R_0 = 1.547$ Å). This hybrid data set for parametrization contains the best of both data sources, with the correct distances and energies from experiment, and an appropriate functional shape and curvature from SW/HF. Figure 3 shows that EDIP fits these scaled HF data extremely well, and also demonstrates the necessity of the variable interaction range. Without the term in a' the intersection between the HF data sets at 1.75 Å forces a poor fit to the equilibrium regions, distorting the density and elastic constants of both phases. Further to this mechanical motivation of a', the lengthening of the interaction with Z as seen in figure 3 is intuitively reasonable as high-coordination phases exhibit increasingly delocalized interactions compared with their short-ranged covalent counterparts.

A comparison with the fixed coordination SW3 and SW4 potentials illustrates a useful interpolation property of the EDIP pair potential. When the parameters β and a' are set to zero, equation (2) reduces to the identical function form of the two SW potentials, thus the situation exists that $U_2(r, 3)$ and $U_2(r, 4)$ are equivalent to the pair terms of SW3 and SW4 respectively.

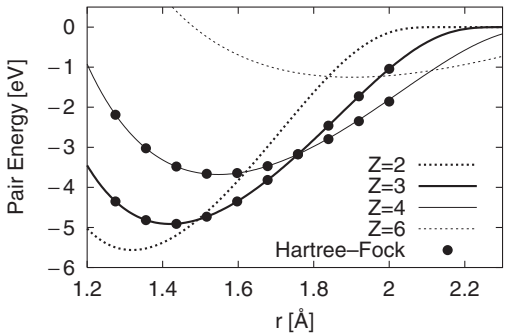

Figure 3. EDIP two-body pair energy for graphite ($Z = 3$) and diamond ($Z = 4$) compared with the scaled *ab initio* data used for the parametrization. Show also are the predictions for carbon in the form of a linear chain ($Z = 2$) and simple cubic structure ($Z = 6$).

Table 1. Quantifying the transferability of EDIP to symmetric structures outside the parametrization. Comparisons are shown with Tersoff [19], OTB [30], LDA/GGA [23] and experimental data [48]. Note that EDIP reproduces the experimental diamond and graphite bond lengths and bond energies by construction as described in the text.

		r_0 (Å)	ε_0 (eV/bond)	ω (cm^{-1})
Dimer	EDIP	1.24	−5.2	1914
($Z = 1$)	Expt	1.24	−6.3	1856
	Tersoff	1.44	−5.0	
	OTB	1.41		
Linear chain	EDIP	1.32	−5.6	
($Z = 2$)	LDA/GGA	1.29	−6.1	
Simple cubic	EDIP	1.89	−1.3	
($Z = 6$)	LDA/GGA	1.76	−1.4	

The EDIP functional form thus provides a means to interpolate between the two HF statepoints, suggestive of considerable applicability in amorphous and liquid systems where coordination states are often non-integer. Outside this range the extrapolation properties of the pair potential are also remarkably good. Table 1 shows that despite being fitted to coordinations three and four, EDIP also proves to have useful transferability to the dimer, linear chain and simple cubic structures. With decreasing coordination the qualitative trends are as expected, with stronger and shorter bonds with decreasing coordination. The only exception is the dimer bond energy, and even for this almost pathological case the properties are far better than other empirical potentials, with the vibrational frequency and bond length agreeing closely with experiment. A significant component of this transferability can be attributed to the bond-order term in the pair potential, confirming the generality of silicon EDIP. A caveat should be added to the simple cubic structure which shows the ideal bond energy when $Z = 6$ identically. When a generalized coordination Z_i is computed (as section 3.3), Z assumes a value less than six, altering the pair and triple energies and leading to values of $r_0 = 1.96$ Å and $\varepsilon_0 = -1.6$ eV.

3.2. Triple interaction

The three-body term follows silicon EDIP in using SW-like radial and angular terms with environmental dependence, but the functional form adopted here is somewhat different to enable direct contact with *ab initio* data and the SW3 and SW4 potentials. The three-body

term is thus written as a product of separable terms in the manner

$$U_3(r_{ij}, r_{ik}, \theta, Z) = \lambda(Z)g(r_{ij}, Z)g(r_{ik}, Z)h(\theta, Z) \tag{3}$$

where the energy penalty vanishes for distances r_{ij} and r_{ik} greater than the pair interaction cutoff of $a + a'Z$. The three components of U_3 are defined by

$$\lambda(Z) = \lambda_0 \exp[-\lambda'(Z - Z_0)^2] \tag{4}$$

$$g(r, Z) = \gamma' \exp[\gamma/(r - a - a'Z)] \tag{5}$$

$$h(\theta, Z) = \frac{1}{q}\{1 - \exp[-q(\cos\theta + \tau(Z))^2]\} \tag{6}$$

where $\tau(Z) \equiv -\cos\theta_0$ describes the variation in ideal bonding angle, following the SW philosophy of an ideal angle θ_0 for which there is no angular penalty. With ideal angles of 180°, 120°, 109.5° and 90° for coordinations two, three, four and six respectively, $\tau(Z)$ is an interpolation function connecting the statepoints $\tau(2) = 1$, $\tau(3) = 1/2$, $\tau(4) = 1/3$ and $\tau(6) = 0$.

The leading term in U_3 is the magnitude function $\lambda(Z)$ which controls the strength of the three-body interactions. The SW/HF data provide values of $\lambda(3) = 71$ eV and $\lambda(4) = 76$ eV, while additional NOTB calculations of a bent linear chain yielded a value of $\lambda(2) = 35$ eV. The Gaussian form of $\lambda(Z)$ (suggested by Bazant [49]) captures the small value of $\lambda(2)$ relative to graphite and diamond, as well as the expected trend of $U_3 \to 0$ for large Z due to diminishing angular importance in metallic systems.

The middle terms in U_3 are the radial functions of equation (5), and as for the pair potential the cutoff in exponential denominator is generalized to include a variable range. It is important that the pair and radial functions terminate identically, as spikes in the RDF can arise if different cutoffs are used for the two distance-based functions. The second reason for including a' is that SW3 and SW4 potentials themselves have radial functions with different cutoffs, and for both coordinations the individual potentials are well fitted by the general EDIP form. Note however, that the radial component data SW/HF is extracted from the HF-parametrized SW potentials, and is not computed directly by HF as for the pair potential.

The final term in U_3 is the angular term $h(\theta, Z)$ capturing the energy cost of distortions away from the ideal angle θ_0. In the limit $q \to 0$ this expression reduces to

$$h_0(\theta, Z) = [\cos\theta + \tau(Z)]^2 \tag{7}$$

which for $\tau(4) = 1/3$ corresponds exactly to the original SW angular form proposed for tetrahedrally bonded silicon [46]. For finite q the angular factor $h_0(\theta, Z)$ still applies for small deviations from the ideal angle, and this important property allows contact between the SW3 and SW4 triple potentials for the case of $U_3(r_{ij}, r_{ik}, \theta, 3)$ and $U_4(r_{ij}, r_{ik}, \theta, 3)$ respectively. The importance of angular softening was identified during the development of silicon EDIP, as without a reduction in angular stiffness for large distortions the liquid state is poorly described. In the case of the Tersoff potential (where there is no angular softening) the melting point of carbon is almost 50% greater than the experimental value [19].

To determine the value of q for EDIP, molecular dynamics simulations of a 2.9 g cm^{-3} liquid were compared with CPMD data at the same density [34]. Note that this was necessarily the final EDIP parameter to be determined. The upper panel of figure 4 shows the equilibrium temperature attained when simple cubic carbon spontaneously collapses and forms a liquid. This temperature of melting reflects the potential energy difference between the simple cubic and liquid states, and is sensitive to angular forces, varying by a factor of two over the range considered. Agreement with the CMPD value of ≈6000 K is seen to be attained for $q = 3.5$. Once the liquid was equilibrated, each sample was rescaled to 5000 K and the diffusion constant

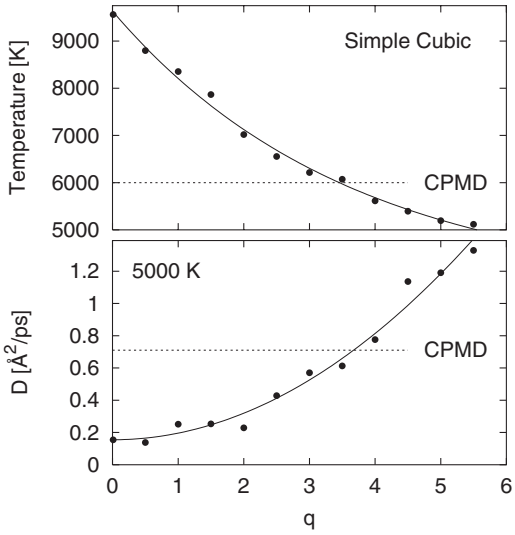

Figure 4. Properties of 2.9 g cm^{-3} liquid carbon computed with EDIP as a function of the angular softening parameter q compared with CPMD calculations [34]. Upper panel: plateau temperature of the liquid following the spontaneous melting of a simple cubic lattice. Lower panel: diffusion constant for liquid carbon at 5000 K. The solid curves are a fit to guide the eye.

Table 2. Elastic constants of diamond and a graphite sheet, in units of GPa. The computed graphite values presume a c-spacing of 3.35 Å. The OTB values are from Xu *et al* [18].

		Expt	EDIP	OTB
Diamond:	B	442	418	456
	$c_{11} - c_{12}$	951	958	622
	c_{44}	576	472	475
Graphite:	$c_{11} + c_{12}$	1232	1233	
	$c_{11} - c_{12}$	880	849	840

was computed for a period of 1 ps. The lower panel indicates there is again a strong dependence on q and agreement with the *ab initio* data is found when $q = 3.5$. The confirmation of the value of q by this second and independent property gives confidence that a softening of angular properties is an appropriate modification to equation (7). Furthermore, the value of q determined by figure 4 describes angular softening very similar to silicon EDIP, illustrating the cross-elemental transferability of the generic EDIP form.

The coordination is exactly three and four for graphite and diamond, and thus U_2 and U_3 determine their elastic constants. Table 2 shows the properties of EDIP compare very favourably with experiment, and in the case of $c_{11} - c_{12}$ for diamond the EDIP prediction is considerably better than OTB. The good performance of EDIP arises from the environment dependence in $\tau(Z)$ which is absent in OTB where a fixed value of the parameter p_σ is used. There are theoretical reasons why $p_\sigma = 3$ is the most appropriate for describing the elastic properties of tetrahedral semiconductors [50], and since $\tau(4)$ corresponds to $p_\sigma = 3$ the behaviour of table 2 follows.

3.3. Coordination counting

The spherical coordination contribution z_i is a function of distance alone, and is determined by the sum $z_i = \sum f(r_{ij})$, where $f(r)$ is a three-parameter function which is unity for $r < f_{\text{low}}$,

zero for $r > f_{\text{high}}$ and between these limits varies continuously according to the expression

$$f(r) = \exp\left(\frac{\alpha}{1 - x^{-3}}\right) \tag{8}$$

where $x = (r - f_{\text{low}})/(f_{\text{high}} - f_{\text{low}})$. In the silicon form of EDIP the coordination Z_i consists solely of a term with this form, with f_{low} and f_{high} chosen intermediate between the first- and second-neighbour distances of the diamond structure. A similar approach is used in the Tersoff and Brenner methods for carbon where the bond-order function is cut off in the vicinity of 2 Å over a range of ≈0.2 Å in width. The differentiating factor for carbon EDIP is that the coordination term (equivalent to a bond-order via $\tau(Z)$ and the term in $-\beta Z^2$) is determined by an implicit fit to *ab initio* data which overcomes unphysical dependences on cutoff parameters such as seen in figure 2.

The second important factor in the coordination term of carbon EDIP is the aspherical term applying for sites with $Z < 4$ which exhibit π-like bonding. The aspects of π-bonding most important to ta-C are the dihedral rotation term (which promotes a locally planar structure), and the non-bonded π-repulsion term, which fixes the equilibrium spacing of graphite and thus prevents the collapse of planar sp^2 units into an artificially dense state. These two mechanisms are necessarily aspherical as they reflect the planar symmetry of graphite and the linear symmetry of sp-bonding, and are included in the generalized coordination Z_i in the manner

$$Z_i = z_i + \pi_3(z_i)X_i^{\text{dih}} + \pi_3(z_i)X_i^{\text{rep3}} + \pi_2(z_i)X_i^{\text{rep2}} \tag{9}$$

where π_2 and π_3 are switching functions identifying two and three-coordinated atoms, and the X_i describe dihedral rotation, π-repulsion at a threefold site and π-repulsion at a twofold site. The functions X_i are zero in the crystalline state, and non-negative otherwise, and thus low-symmetry configurations are penalized with an increased coordination corresponding to a reduction in π character. The coordination increment is described by vector products which capture the appropriate symmetries via the functions

$$X_i^{\text{dih}} = Z_{\text{dih}} \sum \pi_3(z_j)(\hat{\boldsymbol{R}}_{jm} \cdot \hat{\boldsymbol{R}}_{ik} \times \hat{\boldsymbol{R}}_{il})^2 C_{ijklm}^{\text{dih}} \tag{10}$$

$$X_i^{\text{rep3}} = Z_{\text{rep}} \sum \pi(z_j)(\hat{\boldsymbol{R}}_{ij} \cdot \hat{\boldsymbol{R}}_{ik} \times \hat{\boldsymbol{R}}_{il})^2 C_{ijkl}^{\text{rep3}} \tag{11}$$

$$X_i^{\text{rep2}} = Z_{\text{rep}} \sum \pi(z_j)[1 - (\hat{\boldsymbol{R}}_{ij} \cdot \hat{\boldsymbol{R}}_{ik})^2] C_{ijk}^{\text{rep2}} \tag{12}$$

where the jkl are neighbours of i, m is a neighbour of j and $\pi(z)$ selects for two- or threefold sites. To avoid various unwanted first- and second-neighbour interactions the X_i include the distance-based cutoff functions C given by

$$C_{ijklm}^{\text{dih}} = p(R_{ij})p(R_{ik})p(R_{il})p(R_{jm}) \tag{13}$$

$$C_{ijkl}^{\text{rep3}} = (R_{ij} - c_0)^2[1 - p(R_{ij})]p(R_{ik})p(R_{il}) \tag{14}$$

$$C_{ijk}^{\text{rep2}} = (R_{ij} - c_0)^2[1 - p(R_{ij})]p(R_{ik}) \tag{15}$$

with the function $p(r)$ equivalent to $f(r)$ except for different end-points p_{low} and p_{high}. Both repulsive cutoffs are identically zero for $R_{ij} > c_0$, and thus c_0 represents the c-spacing of graphite. The two switching functions $\pi_x(z)$ are polynomials of the form $[(z - x)^2 - 1]^2$ for $|z - x| < 1$ and zero otherwise, while the third switching function $\pi(z)$ is equal to $\pi_3(z)$ for $z > 3$ and unity elsewhere.

The HF data were used to determine Z_{dih}, while the remaining seven parameters were derived from static DFT calculations describing the continuous transformation between diamond and rhombohedral graphite [51]. These data are very useful as they implicitly describe fractional coordination in a range of structures where all atoms are equivalent by symmetry to

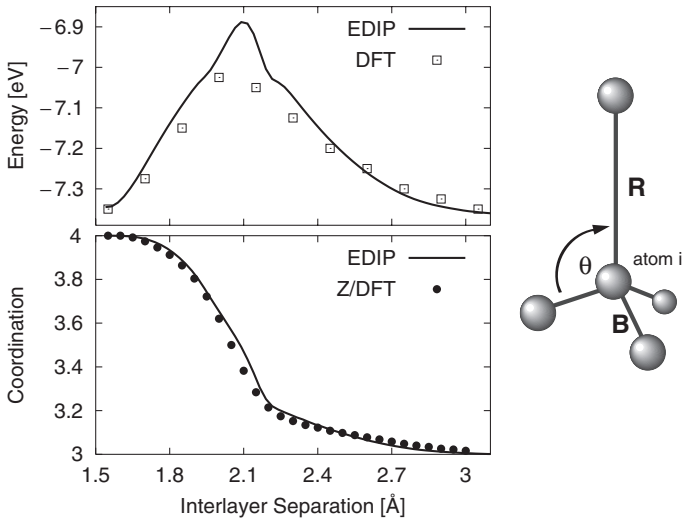

Figure 5. Activation barrier (top) and fractional coordination for the transformation between diamond and rhombohedral graphite as a function of the interlayer separation R. The ball-and-stick fragment illustrates the symmetry shared by all atoms during the transformation. The DFT data are taken from [51], while the points Z/DFT are inferred as described in the text. Energies are per atom.

atom i indicated in figure 5. The DFT reaction path was determined by minimizing the total energy with respect to the in-plane distance B and the inter-planar angle θ for various values of R, and the white squares in figure 5 indicate the energy barrier for the transformation. To make use of these data in the parametrization of EDIP an auxiliary data set Z/DFT is constructed by requiring that the pair and triple potentials together with a numerically determined coordination Z' reproduce the DFT energy barrier. This amounts to solving the implicit equation

$$\Delta U_{\mathrm{EDIP}}(R, B_{\min}, \theta_{\min}, Z') = \Delta U_{\mathrm{DFT}}(R) \tag{16}$$

where Z' is the fractional coordination between three and four, and $B_{\min}$ and $\theta_{\min}$ minimize ΔU_{EDIP} and are functions of R and Z'. Equation (16) is effectively a postulate that the intermediate electronic states can be described by a single quantity, the coordination $Z'(R)$, and comparison of the derived values of $B_{\min}(R, Z')$ and $\theta_{\min}(R, Z')$ with DFT confirms the validity of this hypothesis. It is thus possible to extract an effective fractional coordination from DFT, enabling an essentially unambiguous parametrization of the EDIP coordination component. The most crucial aspect of the Z/DFT data is the sharp change in slope near $R = 2.1$ Å, which partitions the fractional coordination into distinct regimes and greatly simplifies the process of parametrization.

For $R < 2.1$ Å the structure is diamond-like, and the energy barrier is dominated by a σ-bond stretch of the interplanar distance. The dominant term in equation (9) is then the spherical coordination term, and thus the parameters of $f(r)$ can be determined by fitting to the $R < 2.1$ Å data. This aspect sets EDIP apart from traditional analytic potentials when an arbitrary choice of cutoff parameters leads to a poor description of bond breaking, and unphysical spikes as in figure 2.

The region $R > 2.1$ Å corresponds to the graphite-like region in which the non-bonded π-orbitals are forced to have increasing overlap as the sheets are brought together. In this region the dominant contribution to the generalized coordination comes from the aspherical terms, principally the sp^2 π-repulsion term $X^{\mathrm{rep}3}$. The repulsion for sp sites makes no contribution due

Table 3. Parameters of EDIP as fitted to the *ab initio* data. Note that γ' is a fictitious parameter as it does not represent a degree of freedom, since it multiples λ_0 as in [26].

Two-body	$\varepsilon = 20.09$ eV	$B = 0.9538$ Å	$\beta = 0.0490$
	$\sigma = 1.257$ Å	$a = 1.892$ Å	$a' = 0.170$ Å
Three-body	$\lambda_0 = 79.34$ eV	$\lambda' = 0.30$	$Z_0 = 3.615$
	$\gamma = 1.354$ Å	$\gamma' = 0.936$	$q = 3.5$
Coordination	$f_{\text{low}} = 1.547$ Å	$f_{\text{high}} = 2.27$ Å	$\alpha = 1.544$
	$p_{\text{low}} = 1.481$ Å	$p_{\text{high}} = 2.0$ Å	
	$Z_{\text{dih}} = 0.30$	$Z_{\text{rep}} = 0.06$	$c_0 = 3.2$ Å

to the selection rule in $\pi_2(z_i)$, while X^{dih} vanishes due to the symmetry of the vector product. The π-repulsion region is thus described by two quantities, the graphite spacing c_0 and the coordination coefficient Z_{rep}. The value of $c_0 = 3.2$ Å is taken from the DFT calculations to ensure a consistent parametrization, but the actual experimental graphite spacing is 3.35 Å, and so the density of EDIP graphite is too high by 4%. The value of Z_{rep} is thus uniquely determined and the agreement between EDIP and Z/DFT is quite good as seen in figure 5.

The remaining two coordination parameters of the generalized coordination describe the neighbour selection function for π-bonds. Since p_{low} describes the maximum length of a bond showing full π-character, its value will lie somewhere between 1.421 and 1.547 Å, and so the midpoint value is used. In the case of p_{high} which describes the terminating point for a fully broken π-bond, a value of 2.0 Å was chosen as this is less than f_{high} and lies close to the peak in the activation barrier. The final component of the generalized coordination is the repulsion increment for a twofold site described by equation (12). This introduces no additional parameters, and serves to prevent chain structures forming with artificially high densities.

The parameter set of EDIP listed in table 3 is thus almost entirely deterministic, with HF and DFT data contributing to the functional form and its parametrization. Execution time is necessarily considerably longer than for silicon EDIP due to the long range of the π-repulsion terms, but EDIP remains orders of magnitude faster than tight-binding and DFT methods.

4. Applications of EDIP

While static and crystalline structures are necessarily the starting point when developing an empirical potential, a more stringent test of transferability is found in the description of disordered and dynamical systems. The following sections present applications of EDIP to liquid quenching and thin-film deposition, and where comparison is possible, excellent agreement with experimental and CPMD data is found. This ability to describe disordered carbon gives confidence in new theories and insights which are developed from the simulations.

4.1. Properties of the liquid state

The first step in a liquid-quench simulation is the generation of the molten sample, and figure 4 showed earlier how an appropriate value of the angular softening parameter q led to excellent reproduction of the CPMD data. To determine the accuracy of EDIP for liquid properties outside the parametrization, simulations of molten carbon were performed at 2.0, 2.6, 2.9 and 3.2 g cm^{-3}. Each simulation contained 125 atoms, periodic boundary conditions were used within an NVE ensemble, and the coordination was measured by counting neighbours within 1.85 Å. The liquid structures were generated from a slightly randomized simple cubic lattice which avoids superheating and nucleation issues due to a

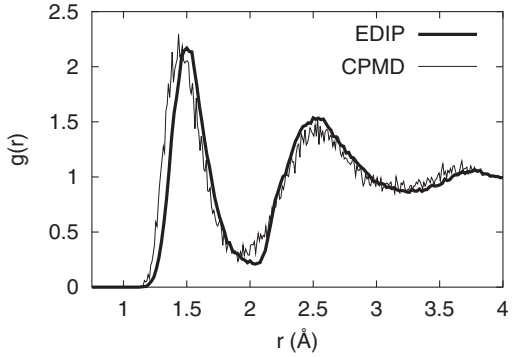

Figure 6. Pair distribution function $g(r)$ for 2.9 g cm^{-3} liquid carbon at 5000 K computed using EDIP and CPMD [52].

destabilizing imaginary phonon mode for tetragonal distortions [38]. With this method the liquid state is attained very quickly ($\sim$50 fs) and thermal averaging at 5000 K for 0.5 ps yields good equilibrium properties.

Figure 6 compares the distribution of distances in the 2.9 g cm^{-3} EDIP simulations with CPMD data at the same density [52], and the overall agreement is very good, reproducing the relative heights of the first and second neighbours, as well as the finite number of distances near 2 Å. Simulations at 2.0 g cm^{-3} find EDIP $g(r)$ again in agreement with CPMD simulations [53], while Tersoff simulations of liquid carbon [19] are qualitatively different as revealed by a decay to zero in the RDF at 2 Å. In figure 6 the small offset of 0.05 Å in the position of the first-neighbour peak can be largely attributed to the coordinated-based formalism which implicitly ascribes to each site a fixed π-conjugation according to the number of neighbours. Consequently, for structural units such as an sp^2 dimer, EDIP will treat both threefold sites as having π-conjugations appropriate for graphite and will therefore overestimate the bond length. A similar effect occurs for twofold-coordinated sites which cannot form triple bonds with length $\approx$1.20 Å, instead favouring double-bond distances as in table 1.

Figure 7 compares the bond-angle distributions for three- and four-coordinated atoms in the 2.9 g cm^{-3} liquid, and as for the distances in figure 6, the agreement is remarkably good, confirming that the transferability observed in the crystalline state extends to non-equilibrium situations. The only difference of note between the angular distributions is the small peak near 60° for four-coordinate atoms. This peak reflects the presence of three-membered rings in the CPMD liquid which are disfavoured in EDIP because the angular penalty function imposes an energy cost approximately twice the strain energy [39]. Tight-binding methods also describe these small rings poorly, and a comprehensive study of small rings by Shultz and Stechel [54] shows that a minimal basis set and restrictive functional form each lead to an overestimation of strain energy for the three-membered ring.

The liquid coordination fractions are a further test for EDIP due to the unusual property of carbon that the liquid has a lower coordination than the solid. This is in contrast to other group IV elements where the converse is the rule, such as for silicon where the liquid coordination is $\approx$6.4. Figure 8 compares the average coordination fraction of the EDIP and CPMD liquids as a function of density, and shows excellent agreement. The time-varying character of the coordination is also well described by EDIP, showing instantaneous fluctuations very similar to those observed by CPMD [53, 55]. The 2.0 g cm^{-3} CPMD simulations defined the coordination cutoff using the first minimum in the RDF, which is slightly larger than the

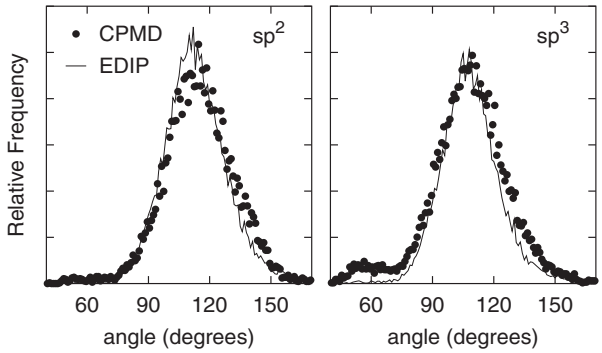

Figure 7. Distribution of angles for threefold sites (sp^2) and fourfold sites (sp^3) in the 2.9 g cm^{-3} liquid carbon samples compared in figure 6. A coordination cutoff of 1.85 Å is used for both EDIP and CPMD.

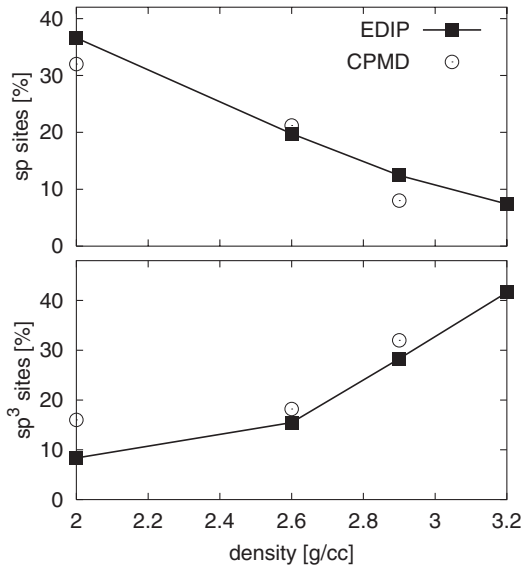

Figure 8. Coordination fractions of the liquid state computed with EDIP simulations and compared with CPMD calculations at 2.0 g cm^{-3} [53], 2.6 g cm^{-3} [37] and 2.9 g cm^{-3} [52]. All data analysis used a bonding cutoff of 1.85 Å, except for the 2.0 g cm^{-3} CPMD simulation which used a larger value (≈2 Å), thus favouring higher sp^3 fractions and smaller sp fractions.

EDIP coordination cutoff. Application of an identical cutoff would reduce the CPMD sp^3 fraction and increase the sp fraction, thereby bringing EDIP into even closer agreement.

The density dependence of the diffusion constant measures transferability away from the parametrization of figure 4. EDIP calculations at 2.0 g cm^{-3} and 5000 K found a diffusion constant of 2.0 $Å^2$ ps^{-1}, which compares very favourably with the value 2.4 $Å^2$ ps^{-1} reported from CPMD [53]. Further agreement is found in the generation of the 2.9 g cm^{-3} liquid, where the time required to collapse the unstable simple cubic lattice was 0.02–0.025 ps for both EDIP and CPMD, indicative of a similar reaction path for the transformation. Overall, the correspondence between EDIP and CPMD is quite substantial, indicating that EDIP provides a useful description of liquid carbon.

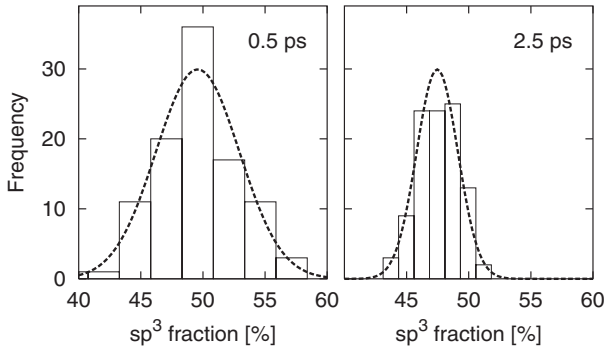

Figure 9. Distribution of sp^3 fractions in one hundred 125-atom EDIP liquid-quench simulations at 2.9 g cm^{-3}. Cooling curves for the 0.5 and 2.5 ps quenches were exponential and linear respectively. Dotted curves indicate the normal distribution with mean and standard deviation of the data sets. The coordination was determined using a bond cutoff of 1.85 Å.

4.2. Liquid quenching

With *ab initio* methods the procedure of liquid quenching is sufficiently burdensome that only a small number of calculations can be carried out at each density. With EDIP however a single quench takes of order 15 min, and so a great many quenches can be performed to evaluate properties such as statistical variability, an important effect considered recently for the first time [39]. In this evaluation of liquid quench statistics, a large number of quench calculations were performed using EDIP at 2.9 g cm^{-3}. Batches of 100 simulations were undertaken, with each quench in the batch using a slightly different configuration for the equilibrated liquid. This was achieved by saving the liquid statepoint prior to each cooling cycle, and then allowing the liquid to evolve for 0.1 ps prior to the subsequent quench. Systems with 64 and 125 atoms were cooled exponentially over a time $t_0 = 0.5$ ps, while a third simulation set contained 125 atoms and was linearly cooled with $t_0 = 2.5$ ps. These three systems are generally representative of liquid-quench calculations in the amorphous carbon literature.

Figure 9 indicates the sp^3 fractions of the equilibrated structures for the two 125-atom scenarios. The average value is just under 50%, in essentially exact agreement with NOTB and slightly less than CPMD. Of even greater significance however is the extent of the statistical variation which had not been previously discussed or measured, and represents an important factor to consider when comparing different preparation conditions and methods. The variability arises from fluctuations in the liquid state at the instant the quench is initiated, as well as the metastable nature of the rapidly quenched structures. Both of these factors are also present in the experimental deposition process, and thus the variability is not an artifact of the simulation technique.

System size is not a key factor determining the sp^3 fraction, as the 64- and 125-atom simulations cooled in 0.5 ps were found to have very similar distributions. The cooling rate however does make a difference to the observed sp^3 fractions. Not only is the distribution of sp^3 values much narrower with the longer cooling, but the mean is reduced with a difference of 1.8–3.2 at the 95% confidence interval. This result helps interpret a number of DFT simulations examining the effect of the cooling rate. In three 64-atom simulations at 2.9 g cm^{-3}, Marks *et al* [52] found that the sp^3 fraction decreased from 68 through 65 to 57% as the quenching time increased, while further 64-atom simulations at 2.9 g cm^{-3} [56] with in principle the same preparation conditions as the 65% sp^3 sample found an sp^3 fraction of ≈55%. In contrast to [52], 125-atom DFT simulations at 3.2 g cm^{-3} [37] observed no cooling rate effect, finding

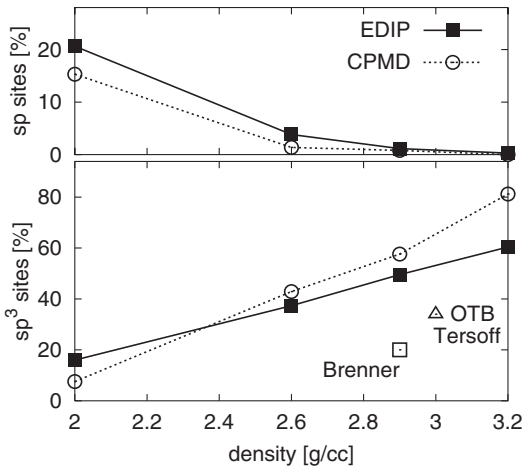

Figure 10. Proportion of two- and four-coordinated sites in networks generated using EDIP and CPMD [37]. The triangle denotes both Tersoff [29] and OTB [30] data which are almost identical. The Brenner data is from [39].

sp^3 fractions of 80.1 and 80.3 for $t_0 = 0.5$ and 1.0 ps respectively. These disparate results can now be understood in the context of the statistical variability evident in figure 9. All of the DFT results lie within the statistical range found using EDIP, and while a cooling rate effect is present, it is not nearly as pronounced as presumed in [52].

As might be anticipated from the sp^3 data, many other quantities in the quench exhibit significant statistical variation. Nearest-neighbour distances, bond angles and ring statistics are important quantities when comparing amorphous networks, and their variation is non-trivial as discussed in [39]. Averaging over multiple quenches is therefore a useful tool for reducing statistical scatter when comparing different levels of theory and preparation conditions. With this principle in mind, multiple EDIP quenches were performed at other densities to evaluate the dependence of coordination on density as in figure 1. Using the liquid networks considered earlier, a minimum of 25 quench simulations were performed at each density, using exponential cooling with $t_0 = 0.5$ ps following by 1 ps of equilibration at 300 K. Figure 10 shows that the coordination fractions of the EDIP structures compare very favourably with those of CPMD. The square and triangular symbols indicate the extent to which the Brenner, Tersoff and OTB methods underestimate the sp^3 fraction in ta-C. In this respect only higher levels of theory such as NOTB and LBDF have better predictive power than EDIP.

Much of the good behaviour of EDIP seen in figure 10 can be traced to the π-repulsion term which gives EDIP graphite its realistic density. Jäger and Albe [43] suggested that the poor description of ta-C with the Brenner and Tersoff potentials might be related to the 'compressed graphite' predicted by both potentials, whereby the short range of the interaction results in a graphitic density similar to that of diamond. This hypothesis is confirmed by EDIP simulations with Z_{rep} set to zero, which show sp^3 fractions very similar to those of OTB and Tersoff. This explains why the Brenner, Tersoff and OTB simulations, none of which have realistic π-repulsion terms, have not been successful in the simulation of ta-C.

Figure 11 shows that across all four densities the distributions of distances in the EDIP networks are in substantial agreement with CPMD structures generated under identical conditions. In particular there are no metastable states in the $G(r)$ intermediate between the first- and second-neighbour distances as found for the Brenner potential in [39] and in figure 2. A minor difference between EDIP and CPMD is observed around 1.3 Å, where the

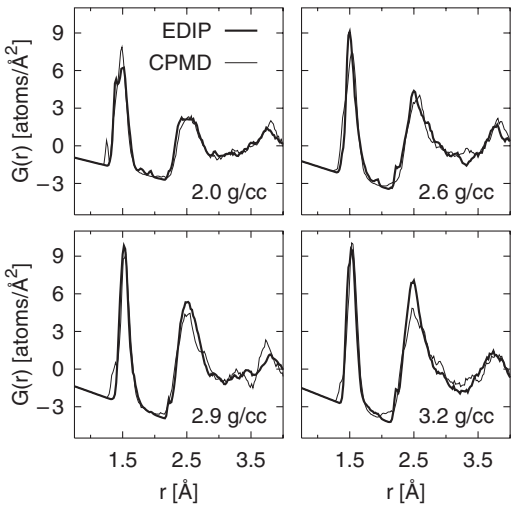

Figure 11. Reduced density function $G(r) = 4\pi r\rho[g(r) - 1]$ for amorphous carbon networks generated by liquid quenching using EDIP and CPMD [37].

treatment of π-conjugation discussed earlier results in an absence of short distances associated with ethylenic-like double bonds. A comparison of bond-angle distributions for 2.9 g cm^{-3} structures in [26] shows for three- and fourfold coordinated sites the agreement between EDIP and CPMD is good, particularly for the sp^2 atoms. For the sp^3 atoms the EDIP distribution is slightly narrower (similar to the liquid as in figure 7), while the positions of the maxima are virtually identical.

Ring statistics for all four networks were computed using the shortest path algorithm of Franzblau [57] and are compared with CPMD in figure 12. Multiple-quench averaging is applied for the EDIP data, but this is not possible for CPMD due to the computational cost involved. The effect of averaging is apparent in the smooth variation of the EDIP data compared with the wide scatter for CPMD. Overall, the two methods predict structures with similar ring distributions, and the presence of agreement for rings with as many as 12 atoms confirms that the EDIP and CPMD networks have considerable topological similarity. The most significant difference between EDIP and CPMD is the near-absence of three- and four-membered rings. The three-membered rings are penalized for energetic reasons as discussed earlier, while a similar argument applies for four-membered rings. The absence of the four-membered rings can also be deduced from figure 11 where the small discrepancy around 2.1 Å arises from the lack of diagonal distances across the carbon quadrilaterals.

One structural difference revealed upon visual inspection of the EDIP networks is the presence of isolated sp^2 atoms. These sites are not unexpected as there is no aspect of the potential which discourages their formation. The presence of these atoms relates to the simplified treatment of conjugation, and results in electronic states at the Fermi level as discussed in [26]. While these details are not insignificant, from a broader structural perspective they are less important than the more general properties which are correctly described such as the distance and angle distribution functions, ring statistics and the dependence of the sp^3 fraction on density. Thus with the liquid and amorphous states well described structurally it can be expected that EDIP will prove capable of describing energetic impact and film deposition.

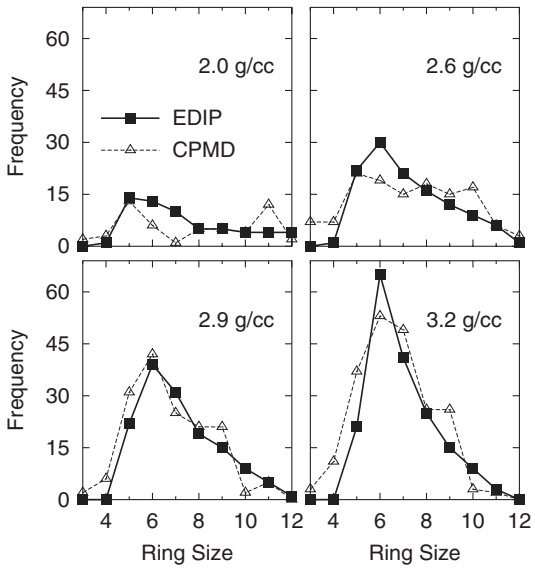

Figure 12. Ring statistics for various densities of amorphous carbons generated using EDIP and CPMD [37]. A cutoff distance of 1.85 Å defines a bond. The EDIP data are averaged over 25 simulations at each density, while the CPMD data describe single configurations.

4.3. Thin-film deposition

Although EDIP is much more efficient than tight-binding methods, the computational cost of modelling deposition remains non-trivial. The simulation of a 40 eV impact lasting 1 ps consumes approximately one hour of CPU time on a workstation, and thus the deposition of a film containing 500 atoms requires several weeks of calculation. Four films were grown using monoenergetic beams with energies of 1, 10, 40 and 100 eV, and each film was deposited onto a room-temperature (001) diamond substrate with (2×1) reconstructed upper and lower surfaces. Periodic boundary conditions were applied in the x- and y-directions, each with a side length of 14.22 Å, and for each energy the 500 atoms are deposited individually onto the upper surface with normal incidence and random position in the xy-plane.

The impact of an energetic species leads to substantial heating of the substrate and film, and thus velocity rescaling wall thermostats of thickness 2 Å acted upon atoms with a lateral displacement greater than 6.11 Å from the initial position of the incident atom. These thermostats prevent recycling of energy through the boundaries, and a similar thermostat applied to the substrate base removes heat which also diffuses away in an infinite system. The motion of all atoms was followed for between 0.5 and 1 ps, and rethermalization to 300 K was carried out prior to deposition of the subsequent atom. This scheme approximates the experimental situation where the time between successive impacts is of order a millisecond, and specifically excludes thermally activated diffusion processes which might possibly contribute to increased surface graphitization. However, the most important interactions occur on the sub-picosecond scale and are fully described.

Figure 13 indicates the coordination of the 40 eV film as a function of depth, showing the top layers of the film ($z \sim 17$) to be sp and sp^2 bonded, in excellent agreement with electron energy loss measurements [58] of 35 eV deposited films which find a 100% π-bonded surface layer with thickness 4 ± 2 Å. Bulk properties of the film are determined for z-values between

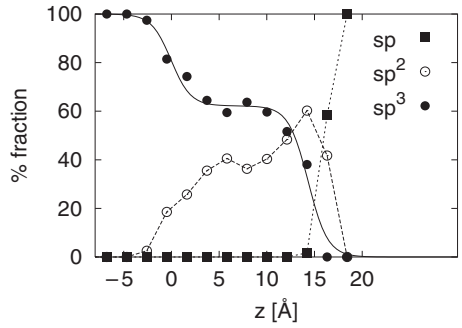

Figure 13. Coordination fractions as a function of depth (z) for the film grown with 40 eV atoms. The solid curve indicates the analytic fit used to identify the bulk region, and the original height of the substrate corresponds to $z = 0$. The coordination cutoff is 1.85 Å.

3 and 11 Å, and indicate the structure is[1] ta-C, with an sp^3 fraction of 61%, a density of 3.17 g cm^{-3} and a biaxial compressive stress of 4.8 GPa. While experiments at this density typically find slightly higher sp^3 fractions (70–80%) and stresses (8–10 GPa), this simulation represents an enormous improvement over the Tersoff and Brenner calculations [42,43] where sp^3 fractions were less than 30% and stresses were not calculated.

Figure 14 shows a ball-and-stick model of the 40 eV film, with the abundance of black atoms denoting sp^3 bonding reflecting the tetrahedral character of the film. Grey atoms indicate sp-bonded atoms which are present only at the surface, forming weakly bonded structures such as loops and chains. At the substrate interface the film does not nucleate uniformly, and a roughness $\approx$3 Å in width is evident due to small amounts of substrate damage and epitaxial growth. The minor degree of epitaxy can also be inferred from the high sp^3 fraction at $z = 0$ in figure 13. In the original surface the atoms in this layer are purely sp^2 (being part of the 2×1 reconstruction), but as the film grows a large fraction of these atoms convert to an sp^3 configuration.

Figure 15 shows the reduced density function for the bulk region of the film. The second-neighbour distances agree well with neutron diffraction data [59], while the first-neighbour peak is somewhat narrower, in part due to the relatively small number of distances available for computing the $G(r)$. This difference is trivial compared with the spurious spikes in the RDF of the Tersoff, modified Brenner and trunctated OTB simulations in figure 2. In the case of EDIP there is no spurious peak because the DFT parametrization of the coordination function provides a correct description of the bond formation and breaking. Other problems related to the RDF were found by Kaukonen and Niemenen whose Tersoff films contained sites with so-called sp^{2+x} and sp^{1+x} bonding. These classifications reflect uncertainty in the interaction cutoff used to define coordination, but in the EDIP calculations there is no such ambiguity as the $G(r)$ drops to the zero-density line $-4\pi\rho r$ close to the coordination cutoff of 1.85 Å.

Figure 16 compares the energy dependence of the EDIP films with the experimental data of McKenzie *et al* [1]. The EDIP properties refer to the bulk region of each film as identified with an analytic fitting function as in figure 13, while the experimental sp^3 fractions were determined using plasmon interpolation [9]. Experimental densities were scaled via the 3.1 g cm^{-3} reference point in [1]. With increasing energy the EDIP films are seen to transform from low-density, tensile stressed a-C at 1 eV, to high-density, compressively stressed ta-C at 40–100 eV. This dependence on deposition energy is very well known from experiments, and

[1] Following [9] which defines ta-C as amorphous carbon with an sp^3 bonding fraction exceeding 50%.

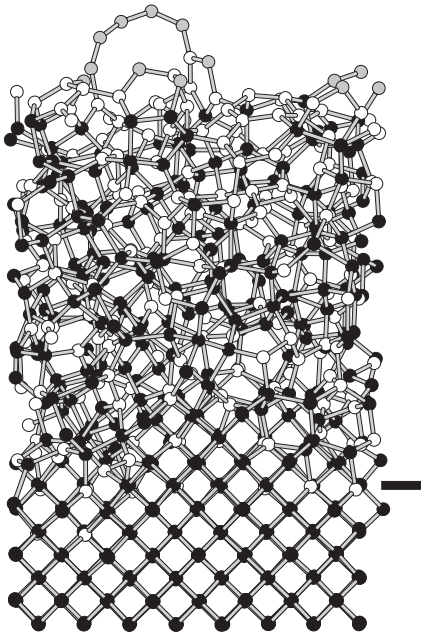

Figure 14. Structure of ta-C thin film deposited with 40 eV atoms. Coordination determined by counting neighbours within 1.85 Å, with grey, white and black circles denoting atoms with two, three and four neighbours respectively. The horizontal bar indicates the initial height of the substrate ($z = 0$ in figure 13).

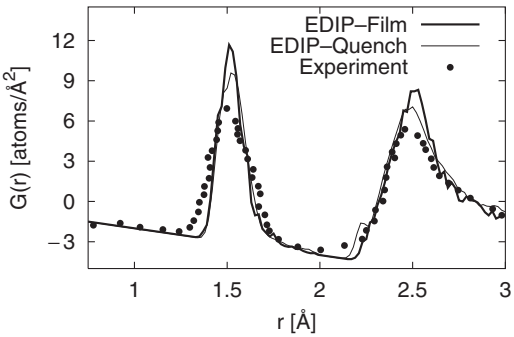

Figure 15. Reduced density function $G(r)$ for the bulk region of the 40 eV film, compared with experimental neutron diffraction of Gilkes *et al* [59] and a 3.2 g cm^{-3} liquid quench.

is reproduced here by simulation for the first time. For each of the films the RDF is physical and reasonable, showing none of the sharp spikes seen in the Tersoff and modified Brenner depositions. No atoms with spurious fivefold coordination were present as in the modified Brenner films [43]. Consistent with experiment, all three quantities in figure 16 share the same systematic variation with energy, in contrast to the simulations of [42] where the maximum sp^3 fraction of 28.5% occurred at 10 eV, while the maximum density was achieved between 40 and 100 eV.

It is useful to consider the minimum energy required to form ta-C, as this provides insight into the physical processes responsible for the tetrahedral bonding. Experimental

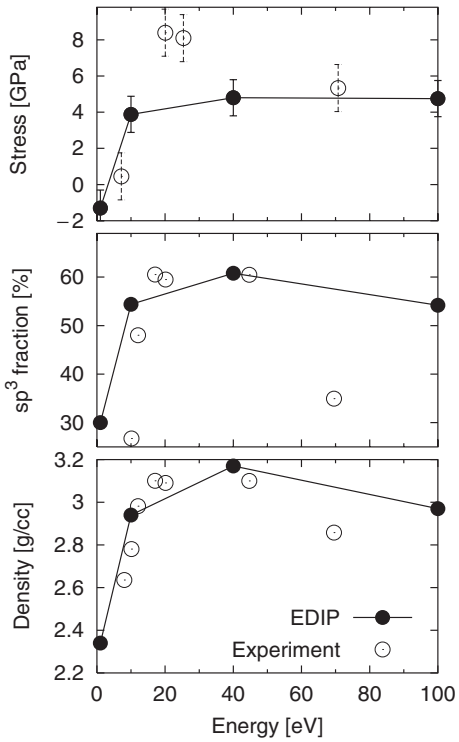

Figure 16. Energy dependence of EDIP-deposited films compared with experimental data of McKenzie *et al* [1]. Error bars for the density and sp^3 fraction lie within the solid circles for both data sets, except for the EDIP 100 eV film where the uncertainty is ≈5%.

determination of this energy is difficult, with a comparison of nine experiments [9] showing a transition from sp^2-rich to sp^3-rich material anywhere between 7 and 30 eV. Defining the precise transition point is further complicated by finite energy linewidths [60] and plasma screening which reduces the energy of the beam relative to the bias voltage. No such ambiguities are present in the EDIP simulations where the ion energies are precisely known, and the simulations shown the threshold energy is less than 10 eV, as at this energy the film grows with 54% sp^3 bonding, and is compressively stressed and dense. The significance of this result lies in the growth mode at 10 eV, which is entirely surface based and does not involve so-called subplantation events as proposed by Robertson [6] and Lifshitz [8]. The mechanism of subplantation proposes that incident species undergo shallow implantation into the sub-surface of the film, leading to densification and sp^3 promotion. This model has emerged over the past decade as the default explanation for tetrahedral bonding and compressive stress in ta-C, in part due to the absence of a potential like EDIP which can probe the deposition process. Since the subplantation model has become part of the framework for interpreting ta-C and a-C experiments, it is appropriate to consider the growth process in more detail.

The nature of the impacts in the four films is analysed in table 4 using the average surface algorithm of [42] with an exclusion radius of 0.77 Å[2]. In agreement with simulation [41, 42] and experiment [61], subplantation processes commence around 40 eV, indicating that the

[2] While [42] used a cylindrical radius of 1.60 Å to identify the surface, 0.77 Å was much more appropriate for the EDIP films.

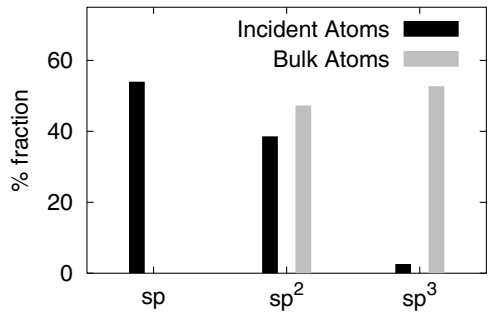

Figure 17. Coordination fractions for the 10 eV film. The black bars describe newly deposited atoms, while grey bars denote atoms in the bulk region of the final film.

Table 4. Impact analysis for the 500 atoms deposited at each energy. The classifications of subplantation, surface and scattering follow [42].

Energy (eV)	Subplantation	Surface	Scattered
1	0	414	86
10	0	485	15
40	12	474	14
100	174	320	6

sp^3-rich 10 eV film grew without subplantation. At the highest energy of 100 eV, the energy required to implant into the film leads to thermal spikes whose annealing effects are evident in figure 16 where the diamond-like properties no longer increase. These subplantation events generate a damage track which leads to a low-density, sp/sp^2 region $\approx$1 nm thick, consistent with experiment [58].

Additional analysis of the 10 eV film confirms the surface-based nature of the growth process at this energy. Figure 17 compares the coordination of newly deposited atoms with those in the bulk once deposition has ceased. If subplantation processes were the origin of diamond-like formation, the grey and black bars would have equal heights for each coordination, a situation which is clearly not the case. Instead, newly deposited atoms locate in surface sites, indicating that the action of deposition buries pre-existing surface, in the process converting the sp/sp^2-rich layer into the predominantly sp^3 bulk. It is therefore evident that ta-C formation is not due to incident species locating themselves underneath pre-existing surface as per subplantation, but rather occurs when existing surface is 'buried'.

The conclusion that the sp^3 bonding is due to a burial process bears considerable resemblance to a 'energetic burial' model developed from the two-dimensional SW3 simulations of carbon film growth [21]. In these simulations films were deposited with energies of 1–100 eV, and excellent agreement with experiment was obtained, with the compressive stress showing the same variation with ion energy as in figure 16. However, no subplantation was observed due to the topology of two dimensions which is much less open than the loosely packed tetrahedral and trigonal structures found in three-dimensional carbon. This observation that compressive stress could be generated without subplantation was an important and unexpected result at the time.

The topological properties of the two-dimensional material were further exploited via a microscopic definition of surface and bulk which is not possible in three dimensions. This distinction enabled precise determination of the growth mode, and showed that the energetic

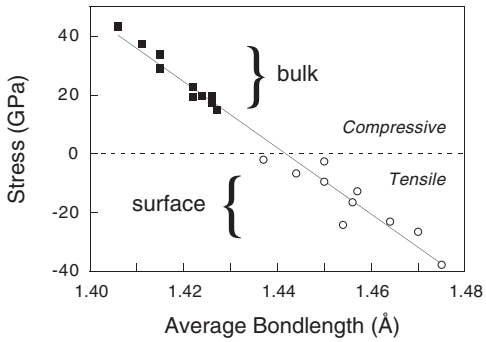

Figure 18. Lateral stress as a function of average bondlength in two-dimensional simulations of deposition using a 50 eV atomic beam [21]. Stress in surface and bulk regions was computed at ten stages during the growth of the film.

incident species converted surface atoms under tensile stress into bulk atoms under compressive stress. The effect of this process of 'energetic burial' is illustrated in figure 18 which shows the stress of the bulk and surface components of a two-dimensional 50 eV film at various stages during its deposition. The surface region of the film is seen to always have long bond-lengths and tensile stress, while the bulk region of the film is seen to always have short bond-lengths and compressive stress. Since all bulk atoms must at some earlier stage be located on the surface, it is only by energetic burial *without subplantation* that compressive stress is created.

The energetic burial model is of direct application to the three-dimensional EDIP simulations, as in this case new atoms locate as sp/sp^2 atoms on the surface, and only upon burial are converted to sp^3 sites. Generalization of the two-dimensional model to three-dimensional carbon therefore indicates that the pressure pulse produced by energetic impact is sufficient to overcome the non-bonded π-repulsion between sp^2 units. As seen in figure 5, DFT calculations show that the activation barrier for graphite–diamond interconversion is 0.33 eV/atom [51], and thus a 10 eV impact is easily capable of providing the energy necessary for the transformation. This process is reminiscent of the sp^3 promotion mechanism in the atomic peening model [10], but bears little resemblance to the thermal spike model [9] as spikes are insignificant in 10 eV impacts. With regard to the other models, further simulations are required to answer the important question of whether the sp^3 fraction and compressive stress are related linearly as suggested by Robertson [6] or have a non-linear relationship consistent with the compressive stress model [11].

Before concluding our discussion of thin-film growth, it is instructive to compare the as-deposited films with the EDIP liquid-quench data considered earlier. In figure 15 the pair distribution function of ta-C prepared by liquid quench is compared with that of bulk ta-C deposited with a 40 eV atomic beam. The structures in the two simulations have very similar distributions of distances despite the different preparation conditions. In particular, although both structures have essentially the same density (3.2 g cm^{-3}), the density in the quench is an input parameter whereas it is an output quantity in the deposition.

The close agreement between liquid quenching and deposited amorphous carbons extends to the sp^3 fraction, whose dependence on density is shown in figure 19. Included in this figure are additional data for films deposited with energies of 2 and 3 eV [62], and liquid-quench simulations at 2.3 g cm^{-3}. Across a broad density range, the sp^3 fractions of the quenched structures share essentially the same linear dependence as the films deposited at varying energy, with an average difference of just 3%. The EDIP simulations are consistent with experiments [2] which show that the sp^3 fraction is a single-valued function of the density

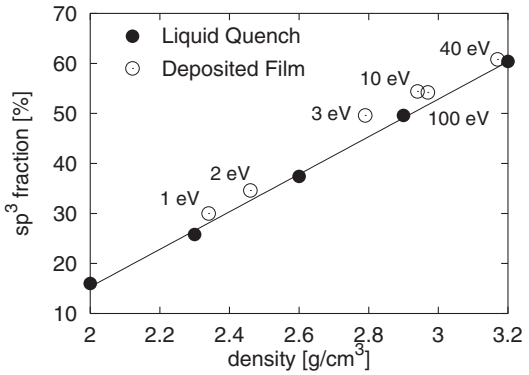

Figure 19. Variation in sp^3 fraction with density in EDIP liquid-quench and deposition simulations. The labels in eV indicate the beam energy used to deposit each film. All of the liquid-quench points are an average of at least 25 simulations, and the uncertainty in the mean is smaller than the data point. The solid curve is a linear fit to the quench data.

as seen in figure 19. The simplest analysis of this experimental data yielded a straight line, but the uncertainties were too great to eliminate the possibility of non-linear relationship between the sp^3 fraction and the density as suggested in [60]. However, with the precision afforded by the multiple liquid-quench simulations the linear relationship is affirmed.

5. Discussion

The case studies of molten carbon, liquid quenching and thin-film deposition provide a comprehensive demonstration of the utility of the EDIP approach. Using the enormous number of references to the Tersoff potential as a guide, it can therefore be anticipated that many other applications in pure carbon systems will follow. In the case of ta-C the effect of temperature on deposition, and Monte Carlo simulations of surface relaxation are just two important problems which are certain to be addressed in an useful manner by EDIP. Perhaps the most surprising aspect of EDIP is the degree of transferability relative to its computational cost. Compared with OTB (at least an order of magnitude more expensive), EDIP provides a vastly better description of disordered carbon, while the traditional empirical carbon potentials of Tersoff, Brenner and SW provide such a poor description of ta-C as to provide very little insight at all.

Given the success of EDIP it is appropriate to consider in what direction its transferability might be extended. In the direction of multi-elemental systems, the most obvious generalization is to a silicon–carbon potential where a number of candidates already exist [63–65], but none have the predictive power of EDIP for the carbon phase. Preliminary investigations into a hybrid SiC potential combining silicon and carbon EDIP via a scaling of the spatial metric show that the elastic constants of the zincblende structure are well described, but the description of the simple cubic phase is inferior to that of the Tersoff SiC potential [63]. This description may well be improved if the silicon EDIP is reformulated (and refitted) using the methodology shown here to be so successful for carbon.

With regards transferability in the pure carbon phase, it would be preferable to reproduce the density of graphite exactly, particularly if this increased the sp^3 fraction at high densities. Stretching the DFT activation barrier to bring the graphitic density in line with experiment might prove useful in this regard. In terms of the on-site formulation it is straightforward to define an average coordination in the manner of Abell [47] for pair interactions, and this approach may be of benefit in situations where mixed-coordination bonding is of particular

interest. Liquid-quench simulations using such an average pair combination exhibited a small spike in the RDF, which is likely due to different coordinations (and thus cutoffs) of the pair and triple potentials. In the on-site formalism however, the pair and triple terms are always robustly defined, and can be mapped to an equivalent SW potential. Without this important property unphysical structures can arise in disordered systems, such as were seen during the development of the analytic BOP [66]. Robustness is therefore essential for modelling the amorphous and liquid states, and together with its good transferability EDIP represents a new direction for carbon empirical potentials.

In summary, this paper has shown how EDIP is parametrized almost entirely deterministically by applying *ab initio* data in high-symmetry configurations. The benefit of this approach is seen in simulations of the liquid and amorphous state where excellent agreement with CPMD data is found, the statistical variability of quenching is quantified, and no unphysical distances are observed as present in Tersoff, Brenner and truncated OTB simulations. In the first simulations of ta-C thin-film deposition the unique combination of efficiency and transferability is demonstrated. Densities, sp^3 fractions and stresses correlate with the incident energy as observed experimentally, and again no unphysical distances or coordinations are present. The widely accepted subplantation model is shown to be inconsistent with the simulations, and a new model of ta-C film growth is proposed in which energetic burial leads to the simultaneous processes of sp^3 promotion, densification, stress generation and surface growth.

Acknowledgments

The development of EDIP has been made possible due to a continued computational programme at The University of Sydney, and the contributions of David McKenzie, Bernard Pailthorpe, Dougal McCulloch, Chris Goringe, Nick Cooper, Pal Goa, Atagun Bensan and Paul Mahon are gratefully acknowledged.

References

[1] McKenzie D R, Muller D and Pailthorpe B A 1991 *Phys. Rev. Lett.* **67** 773
[2] Fallon P J, Veerasamy V S, Davis C A, Robertson J, Amaratunga G A J, Milne W I and Koskinen J 1993 *Phys. Rev.* B **48** 4777
[3] Lifshitz Y, Kasi S R and Rabalais J W 1990 *Mater. Sci. Forum* **52/53** 237
[4] Ogtana K, Andoh Y and Kamijo E 1988 *Nucl. Instrum. Methods Phys. Res.* B **33** 635
[5] Schwan J, Ulrich S, Theel T, Roth H, Ehrhardt H, Becker P and Silva S R P 1997 *J. Appl. Phys.* **82** 6024
[6] Robertson J 1993 *Diamond Relat. Mater.* **2** 984
Robertson J 1994 *Diamond Relat. Mater.* **3** 361
[7] Davis C A 1993 *Thin Solid Films* **226** 30
[8] Lifshitz Y, Kasi S R and Rabalais J W 1989 *Phys. Rev. Lett.* **68** 1290
Lifshitz Y, Kasi S R, Rabalais J W and Eckstein W 1990 *Phys. Rev.* B **41** 10 468
[9] Hofsäss H, Feldermann H, Merk R, Sebastian M and Ronning C 1998 *Appl. Phys.* A **66** 153
[10] Koponen I, Hakovirta M and Lappalainen R 1995 *J. Appl. Phys.* **78** 5837
[11] McKenzie D R 1996 *Rep. Prog. Phys.* **59** 1611
[12] Ferrari A C, Kleinsorge B, Morrison N A, Hart A, Stolojan V and Robertson J 1999 *J. Appl. Phys.* **85** 7191
[13] Friedmann T A, Sullivan J P, Knapp J A, Tallant D R, Follstaedt D M, Medlin D L and Mirkarimi P B 1997 *Appl. Phys. Lett.* **71** 3820
[14] Car R and Parrinello M 1985 *Phys. Rev. Lett.* **55** 2471
[15] Sankey O F and Niklewski D J 1989 *Phys. Rev.* B **40** 3979
[16] Porezag D, Frauenheim T, Köhler Th, Seifert G and Kaschner R 1995 *Phys. Rev.* B **51** 12 947
[17] Wang C Z, Chan C T and Ho K M 1991 *Phys. Rev. Lett.* **66** 189
[18] Xu C H, Wang C Z, Chan C T and Ho K M 1992 *J. Phys.: Condens. Matter* **4** 6047
[19] Tersoff J 1988 *Phys. Rev. Lett.* **61** 2879
[20] Brenner D W 1990 *Phys. Rev. Lett.* **42** 9458
Brenner D W 2000 *Phys. Status Solidi* b **216** 23

[21] Bensan A 1990 *Honours Thesis* The University of Sydney
Marks N A, McKenzie D R and Pailthorpe B A 1996 *Phys. Rev.* B **53** 4117
[22] Mahon P, Pailthorpe B A and Bacskay G B 1991 *Phil. Mag.* B **63** 1419
Pailthorpe B A 1991 *J. Appl. Phys.* **70** 543
[23] Tang M S, Wang C Z, Chan C T and Ho K M 1996 *Phys. Rev.* B **53** 979
[24] Pettifor D G and Oleinik I I 1999 *Phys. Rev.* B **59** 8487
Oleinik I I and Pettifor D G 1999 *Phys. Rev.* B **59** 8500
[25] Nguyen-Manh D, Pettifor D G and Vitek V 2000 *Phys. Rev. Lett.* **85** 4136
[26] Marks N A 2001 *Phys. Rev.* B **63** 035401
[27] Justo J F, Bazant M Z, Kaxiras E, Bulatov V V and Yip S 1998 *Phys. Rev.* B **58** 2539
[28] Marks N A 1997 *Phys. Rev.* B **56** 2441
[29] Stephan U and Haase M 1993 *J. Phys.: Condens. Matter* **5** 9157
[30] Wang C Z and Ho K M 1993 *Phys. Rev. Lett.* **71** 1184
Wang C Z and Ho K M 1994 *Phys. Rev.* B **50** 12 429
[31] Stephan U, Frauenheim Th, Blaudeck P and Jungnickel G 1994 *Phys. Rev.* B **50** 1489
Frauenheim Th, Blaudeck P, Stephan U and Jungnickel G 1993 *Phys. Rev.* B **48** 4823
Frauenheim Th, Jungnickel G, Stephan U, Blaudeck P, Deutschmann S, Weiler M, Sattel S, Jung K and Ehrhardt H 1994 *Phys. Rev.* B **50** 7940
[32] Drabold D A, Fedders P A and Stumm P 1994 *Phys. Rev.* B **49** 16 415
[33] Hutter J, Alavi A, Deutsch T, Bernasconi M, Goedecker St, Marx D, Tuckerman M and Parrinello M 1995–2001 *CPMD Code* MPI fur Festkorperforschung and IBM Zurich Research Laboratory
[34] Marks N A, McKenzie D R, Pailthorpe B A, Bernasconi M and Parrinello M 1996 *Phys. Rev. Lett.* **76** 768
[35] Clark S J, Crain J and Ackland G J 1997 *Phys. Rev. Lett.* **55** 14 059
[36] Drabold D A, Fedders P A and Grumbach M P 1996 *Phys. Rev.* B **54** 5480
[37] McCulloch D G, McKenzie D R and Goringe C M 2000 *Phys. Rev.* B **61** 2349
[38] Schultz P A, Leung K and Stechel E B 1999 *Phys. Rev.* B **59** 733
[39] Marks N A, Cooper N C, McKenzie D R, McCulloch D G, Bath P and Russo S P *Phys. Rev.* B submitted
[40] Kaukonen H-P and Nieminen R M 1992 *Phys. Rev. Lett.* **68** 620
[41] Uhlmann S, Frauenheim Th and Lifshitz Y 1998 *Phys. Rev. Lett.* **81** 641
[42] Kaukonen M and Niemenen R M 2000 *Phys. Rev.* B **61** 2806
[43] Jäger H U and Albe K 2000 *J. Appl. Phys.* **88** 1129
[44] Fagan M, Marks N A, Cooper N C and Goringe C M, in preparation
[45] Kohary K and Kugler S 2001 *Phys. Rev.* B **63** 193404
[46] Stillinger F and Weber T A 1985 *Phys. Rev.* B **31** 5262
[47] Abell G C 1985 *Phys. Rev.* B **31** 6184
[48] Martin J M L, El-Yazal J and François J P 1995 *Chem. Phys. Lett.* **242** 570
[49] Martin Bazant 1997 *PhD Thesis* Harvard University
[50] Bazant M Z and Kaxiras E 1997 *Phys. Rev.* B **56** 8542
[51] Fahy S, Louie S G and Cohen M L 1986 *Phys. Rev.* B **34** 1191
[52] Marks N A, McKenzie D R, Pailthorpe B A, Bernasconi M and Parrinello M 1996 *Phys. Rev.* B **54** 9703
[53] Galli G, Martin R, Car R and Parrinello M 1989 *Phys. Rev. Lett.* **62** 555
Galli G, Martin R, Car R and Parrinello M 1990 *Phys. Rev.* B **42** 7470
[54] Schultz P A and Stechel E B 1998 *Phys. Rev.* B **57** 3295
[55] Marks N 1997 *PhD Thesis* The University of Sydney
[56] McCulloch D G 1999 private communication
[57] Franzblau D S 1991 *Phys. Rev.* B **44** 4295
[58] Davis C A, Amaratunga G A J and Knowles K M 1998 *Phys. Rev. Lett.* **80** 3280
[59] Gilkes K W R, Gaskell P H and Robertson J 1995 *Phys. Rev.* B **51** 12 303
[60] Lossy R, Pappas D L, Roy R A, Doyle J P, Cuomo J J and Bruley J 1995 *J. Appl. Phys.* **77** 4750
[61] Lifshitz Y, Lempert G D and Grossman E 1994 *Phys. Rev. Lett.* **72** 2753
[62] Marks N A *Phys. Rev.* B in preparation
[63] Tersoff J 1989 *Phys. Rev.* B **39** 5566
Tersoff J 1994 *Phys. Rev.* B **49** 16 349
[64] Dyson A J and Smith P V 1996 *Surf. Sci.* **355** 140
Dyson A J and Smith P V 1999 *Mol. Phys.* **96** 1491
[65] Shimojo F, Ebbsjö I, Kalia R K, Nakano A, Rino J P and Vashishta P 2000 *Phys. Rev. Lett.* **84** 3338
[66] Pettifor D G and Oleinik I I 2000 *Phys. Rev. Lett.* **84** 4124